Highlights

Characterizing the instability limits of turbulent, premixed combustion using CO_2-diluted, oxy-methane/hydrogen mixtures

Mauro Daese, Francesco Contino, Joshua Lacey

- Oxy-fuel combustion nullifies NOx emissions and can valorise O_2 produced from electrolysis.

- The increased O_2 concentration in the oxidizer mixture is leading to a total increase of indicated efficiency, even when operating in a significantly CO_2 diluted environment.

- The increased H_2 concentration in the fuel mixture is leading to a total increase of indicated efficiency, even when operating in a significantly CO_2 diluted environment.

- The CO_2 dilution limit of the oxy-CH_4/H_2 combustion event is captured by the premixed combustion theory when compared against an experimental measurement of combustion instability.

Characterizing the instability limits of turbulent, premixed combustion using CO_2-diluted, oxy-methane/hydrogen mixtures

Mauro Daese[a,b,*], Francesco Contino[a], Joshua Lacey[b]

[a]*Department of Mechanical Engineering, KU Leuven, Celestijnenlaan 300, Leuven, 3001, Belgium*
[b]*Institute of Mechanics, Materials and Civil Engineering (iMMC), Place du Levant 2, Louvain-la-Neuve, 1348, Belgium*

Abstract

This study investigates the combustion instability limits of CO_2-diluted oxy-methane/hydrogen mixtures in a spark ignition engine through a combined experimental and numerical approach. Two experimental campaigns were conducted at constant fuel mean effective pressure and maximum brake torque spark timing. In each campaign, either the oxidizer composition was varied while the fuel mixture remained fixed, or vice versa. These experiments were designed to provide insight into combustion phenomena across a broad spectrum of fuel and oxidizer mixtures representing a wide range of thermophysical properties, and to explore regimes not typically encountered in reciprocating engines operated with air. Over the series of tested conditions, the pronounced thermal quenching effect of CO_2 causes a shift in the cyclic energy balance. While the replacement of N_2 with CO_2 in the oxidizer causes a reduction in thermal efficiency, proportionally more heat is distributed to the combustion chamber gases, suggesting a combined heat and power application, which in principle could produce zero NO_x, would be most appropriate for this concept. The experimental results were then used to extend the theory of premixed, turbulent combustion to the CO_2-diluted oxy-fuel regime. The interaction between turbulent flame propagation and the in-cylinder mixture was further analyzed using predictive modeling and compared to established theories of premixed, turbulent combustion. The results demonstrate that the dilution limit of oxy-CH_4/H_2 combustion based on theoretical predictions correlate strongly experimental measurements of combustion instability, even in cases when the engine operation appears to deviate from the flamelet regime.

Keywords: CO_2 dilution, oxy-fuel combustion, laminar flame speed, premixed turbulent combustion theory, hydrogen

1. Introduction

Achieving net-zero emission of greenhouse gases by 2050 will necessitate a shift towards renewable sources of power generation [1], though the intermittency of these sources guarantees that there will always be a demand for dispatchable power during times of peak demand. Reciprocating engine power plants are one option to address this demand and there is currently an installed capacity of 30 GW of such engines in the EU, equivalent to roughly 15% of the current installed wind capacity across the member states. Due to their high dispatchability and ramping capabilities, the internal combustion (IC) engine power plant is an ideal technology for peaking and grid stability [2]. However, such engine power plants operate with fossil fuels, thus emitting CO_2 and other pollutants such as oxides of nitrogen (NOx) [3]. While most NOx compounds contribute primarily to air pollution, it is specifically N_2O that has a significant greenhouse gas warming potential (GWP). Oxy-fuel combustion is a potential solution to mitigate pollutant emissions from reciprocating engines, as the fuel is in the presence of oxygen rather than air, eliminating N_2 in the intake mixture and therefore avoiding NO_x formation. Additionally, such engines can directly valorize streams of O_2 produced after water electrolysis for green hydrogen production [4]. While CO_2 is still emitted when combusting hydrocarbon fuels, such as natural gas, the high concentration of CO_2 in the exhaust compared with conventional combustion (10% vs. 70%) greatly reduces the cost and complexity of carbon-capture [5, 6]. When considering the valorization of e-methane using captured CO_2, a method for long-term seasonal storage in highly renewable grids [7, 8, 9], the capture of CO_2 emissions from an oxy-fuel engine would result in sustainable power generation. Though there are promising opportunities, oxidizing CH_4 at stoichiometry with pure oxygen (without N_2 as thermal buffer) would result in excessively high peak combustion temperatures in a range of 2500°C to 3000°C [10], which would likely result in damaging the engine [11]. Researchers have investigated various diluent options to mitigate this issue, such as H_2O, Ar and CO_2 [12, 13, 14, 15]. Among these choices, CO_2 is economically interesting for an oxy-fuel reciprocating engine operating with methane, as it can be recycled from the combustion products by condensing out water in the exhaust. However, the use of CO_2 dilution has a number of disadvantages that are exacerbated when combined with methane flames, given their relatively low flame speed compared to other hydrocarbon fuels. Since CO_2 has a higher molar specific heat capacity, meaning it can absorb more heat without a rapid temperature rise, and a higher density than nitrogen or argon, making it harder to push the flame front

*Mauro Daese: Celestijnenlaan 300, Leuven, 3001, Belgium.
Email address: mauro.daese@kuleuven.be (Mauro Daese)

forward, it slows flame propagation. This extends the combustion event duration and increases the time available for heat losses [12, 16, 17]. One possibility to overcome the inherent thermophysical disadvantages of CO_2-diluted combustion with CH_4, as well as an improvement for its carbon intensity, is to enrich the fuel mixture with hydrogen. It is well established that hydrogen has low ignition energy , a large flammability range and has a high flame speed [18], therefore the addition of H_2 to CH_4 acts to partly mitigate the negative effects from CO_2 dilution. This also has the obvious benefit of decreasing the carbon-intensity of the power and heat generated by the engine, and could become an option in power-to-x scenarios where hydrogen is produced from excess renewable energy and injected into the gas grid [19].

To date, there has been limited study of premixed oxy-fuel combustion in reciprocating engines. Experimental work conducted several decades ago was focused on non-premixed, compression ignition engines [20, 21], most of which were intended for the propulsion of unmanned submersibles [22, 23, 24, 25] and unsurprisingly concluded that it is not economically feasible for transport applications. There are several numerical investigations of premixed, SI oxy-fuel combustion considering CO_2 or EGR dilution and water injection [26, 27, 28], and experimentally, stoichiometric SI oxy-CH_4 studies with flame speed predictions were performed by Van Blarigan et al. [12, 16]. While such work identified the practical challenges of CO_2-diluted oxy-methane combustion, there is currently no generalized understanding of instability limits when utilizing non-air oxidizer gas mixtures.

This aspect is particularly important because oxy-fuel combustion mixtures are heavily diluted, which leads to inherently slower combustion and extended flame durations. Moreover, there is no existing study for mixtures of CH_4 and H_2 in the oxy-fuel environment of a reciprocating engine. The inclusion of H_2 in the fuel mixture has the obvious practical benefit of improving CO_2-diluted oxy-fuel combustion performance due to high flame speed and reduced carbon intensity, but perhaps more importantly, it allows for a deeper insight into the limits of reacting flows achievable in a reciprocating engine environment across a wide range of oxidizer mixtures and fuel properties, described through the framework of premixed, turbulent combustion. Such knowledge is essential to realize future oxy-fuel engines for power generation. Therefore, the current work seeks to provide a detailed characterization of CO_2-diluted oxy-fuel combustion in an SI engine using mixtures of methane and hydrogen. The work will utilize reduced-order modeling and fundamental, premixed turbulent combustion theory [29, 30] to attempt to relate an experimentally measured quantity representative of instability to bulk-flame quenching predictions of theoretical computation. Though this effort, the current work will determine if there is broad applicability of such theory to describe oxy-fuel combustion in combustion chamber scenarios that depart significantly from typical fuel-air combustion in terms of thermophysical mixture properties.

2. Experimental setup

The experiments are conducted on a single-cylinder spark-ignition (SI) engine, specifically adapted for oxy-fuel combustion. This engine is a modified version of a single-cylinder Yanmar diesel generator. Detailed engine specifications are listed in Table 1, while the test bench layout is depicted in Figure 1. Several alterations were made to the cylinder head to accommodate a spark plug, a thermocouple, and an in-cylinder pressure sensor. The engine's compression ratio was decreased to 9.8 from its original factory setting, and the valve timing was revised to eliminate overlap. These changes were implemented to prevent autoignition in oxygen- and hydrogen-enriched environments and to minimize the recirculation of residual gases. Ignition timing (IT) is managed through a MoTeC M84 electronic control unit (ECU). In-cylinder pressure is monitored using a high-frequency AVL GH15D piezoelectric pressure sensor, with signal amplification provided by an AVL FlexIFEM 2P2E unit. Fuel and oxidizer mass flow rates are precisely controlled via Brooks SLA-585x series mass flow controllers (MFCs). Pressures of the intake mixture and exhaust gases are

Table 1: SI engine used for experimentation.

Engine type	Air-cooled Single-cylinder
Make	Yanmar L100V
Displacement [L]	0.4357
r_c	9.8
Bore (b) [mm] · Stroke (L) [mm]	86 · 75
Connecting rod length (l) [mm]	120.5
Crack radius (c_r) [mm]	37.5
IVO [CAD]	0 ATDC
IVC [CAD]	233 ATDC
EVO [CAD]	-233 ATDC
EVC [CAD]	0 ATDC

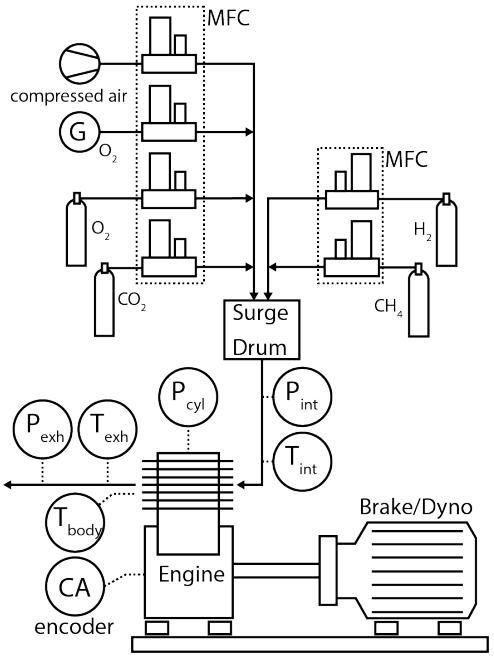

Figure 1: Experimental setup schematic

measured with KISTLER 4260 pressure transducers. Temperature measurements of the intake mixture, exhaust gases, and the engine's external cylinder wall are taken using three K-type thermocouples. An electric motor, connected to the engine's crankshaft, ensures a stable operational speed of 1500 RPM-typical of stationary generator sets designed to produce electricity at 50 Hz. Torque is measured using a flange-mounted HBM T40B torque sensor located on the shaft linking the motor and engine. A Heidenhain ROD 426 crank angle encoder, capable of capturing 3600 samples per revolution, is used to determine crank angle positions and synchronize the acquisition of in-cylinder pressure data. All raw data is logged through an NI cRio 9022 data acquisition module. Depending on engine demand, oxygen is supplied either from a high-pressure cylinder (for low flow rates) or from a Noxerior OP-60 Ecoline PSA oxygen generator (for higher flow rates), capable of delivering 95% pure O_2. Uncertainties in the experimental data arise from various sources, including the MFC readings, gas purity, crank angle position measurements, in-cylinder pressure signals, and pressure sensors on the intake and exhaust sides. A detailed summary of these uncertainties is presented in Table 2. In this table, FS refers to the full-scale reading and PV denotes the processed value. The approach followed for this uncertainty analysis is based on the methodology described by Pochet et al. [31].

Table 2: Summary of equipment uncertainty.

Equipment	Parameter	Uncertainty / Value
MFC (Brooks SLA585X)	Accuracy	±0.7% PV
	Repeatability	±0.2% FS
	Temp. zero drift	±0.05% FS/K
	Temp. span drift	±0.05% FS/K
	Pressure drift	±0.429% PV/Bar
Gas cyl. (Air Liquide)	CH_4	99.5%
	O_2	99.995%
	CO_2	99.995%
Heidenhain ROD 426	Least Count	0.1 CAD
	TDC positioning	±0.05 CAD
AVL GH15D + FlexIFEM	Amplifier accuracy	±0.01% FS
	$\text{Accuracy}_{G,amp}$	±0.5% (U95)
KISTLER 4260	Linearity + Repeat.	±0.2% FS
	Age drift	±0.1% PV/year
	Temp. drift	±1.5% PV

3. Methodology

This section first presents the operating conditions explored in this study and introduces the primary experimental parameters. This is succeeded by an explanation of a reduced-order model developed in GT-Power, which is for heat release analysis and predictive modeling of the combustion process. Particular emphasis is placed on the methodology for extracting essential parameters from the numerical model to facilitate the application of relevant premixed turbulent combustion theory. The first experimental series feature pure CH_4 while systematically varying the oxidizer composition to progressively increase the oxygen content. Conversely, the second campaign maintains a constant oxidizer mixture and gradually blends H_2 into the fuel, beginning with pure CH_4 and incrementally increasing the hydrogen proportion.

3.1. Experimental operating conditions

The non-dimensional fuel/oxidizer mixture strength used in the experiments is defined by the ratio λ'. In principle, this ratio is similar to the equivalence ratio for the conventional combustion process, however, only O_2 is considered and a different notation is used because the oxidizer is, in general, a mixture of gases other than air.

$$\lambda' = \frac{1}{\phi'} = \frac{\frac{\dot{m}_{O_2}}{\dot{m}_{fuel}}}{\left\{\frac{\dot{m}_{O_2}}{\dot{m}_{fuel}}\right\}_{stoichiometric}} \tag{1}$$

In Equation 1, $\dot{m}_{O_2}$ represents the flow of O_2 and $\dot{m}_{fuel}$ represents the flow of fuel into the engine cylinder in kg/s. For fuel blends of methane and hydrogen, the resulting λ' can be calculated as the harmonic mean:

$$\lambda' = \frac{1}{\phi'} = \frac{1}{\frac{1}{\lambda'_{CH_4}} + \frac{1}{\lambda'_{H_2}}} \tag{2}$$

Table 3 presents 15 selected operating conditions, divided in three subsets, chosen from the complete experimental dataset to capture the full spectrum of engine behavior tested in this study. Much of the analysis in this work centers on the first ten conditions, while operating points 11 through 15 are reserved for Section 5 during the discussion of premixed turbulent combustion. The volume fractions of CO_2, O_2 and N_2 in the oxidizer are represented by V_{CO_2}, V_{O_2} and V_{N_2}, respectively, while E_{H_2} denotes the energy-based fraction of H_2 in the fuel blend. In addition, Table 3 includes five supplementary operating points drawn from another test series that focuses on the transition from conventional CH_4-air combustion to oxy-fuel CH_4 combustion as N_2 is replaced with CO_2. Operating condition 3, 6 and 15 represent the same operating condition, this is the central operating linking the three different experimental campaigns. Throughout all experiments, the input energy from the fuel is held constant. This is quantified by the fuel mean effective pressure (fuelMEP), a pressure-based metric that represents the fuel energy delivered per cycle, normalized by the engine's displacement volume [32]. For all operating conditions the fuelMEP is held constant and set to 25 Bar. During the first experimental campaign, the injected fuel energy was held constant while the oxidizer composition was varied. Consequently, an increase in oxygen content led to a corresponding rise in λ'. By contrast in the second campaign, the oxidizer composition remained fixed while the fuel mixture was adjusted, allowing λ' to remain constant. Given that the engine is air-cooled, its thermal condition was carefully monitored throughout the experiments using thermocouples mounted on the body of the engine. This limitation restricted operation when approaching stoichiometric conditions under high oxygen or hydrogen enrichment, and hence the focus on the specific experimental conditions previously outlined. Thermal cut-off limits were established at 200°C for the engine block and 110°C for the oil. Beyond these limits, the associated heat losses became substantial,

Table 3: Operating conditions

Sl. No.	E_{H_2}	V_{N_2}	V_{O_2}	V_{CO_2}	λ'	IT (BTDC)
1	0	0	30	70	1.45	41
2	0	0	33	67	1.59	38
3	0	0	36	64	1.73	37
4	0	0	45	55	2.17	34
5	0	0	60	40	2.89	27
6	0	0	36	64	1.73	37
7	10	0	36	64	1.71	28
8	25	0	36	64	1.73	23
9	50	0	36	64	1.75	16
10	75	0	36	64	1.74	10
11	0	79	21	0	1	21
12	0	56	25	19	1.17	27
13	0	36	28	36	1.35	31
14	0	17	32	51	1.53	34
15	0	0	36	64	1.73	37

making further testing impractical. The upper bound of hydrogen fraction in the fuel mixture was limited to 75% in order to prevent backfire phenomena that were observed for pure hydrogen operation at the fixed fuelMEP of the experiments. During experimentation, the engine's intake pressure is maintained at atmospheric pressure to simulate full load conditions typical of a naturally aspirated engine. This is achieved by running the engine near the maximum brake torque (MBT) while varying ignition timings (IT). The optimal IT is identified at MBT, where the peak in-cylinder pressure occurs at 15 crank angle degrees after top dead center (15 CAD ATDC) according to [32], and is validated experimentally by observing IMEP trends over a range of spark timings. Throughout the experiments, the fuel mean effective pressure (fuelMEP) remains constant, while λ', V_{CO_2}, and E_{H_2} are adjusted accordingly.

3.2. Analysis of the experimentally measured in-cylinder pressure trace

For each operating condition, a subset of pressure traces is selected based on median values of IMEP, peak pressure, and peak pressure position. Among these, the pressure trace closest to the mean pressure profile is chosen for detailed post-processing by evaluating the root mean square error (RMSE) over the closed portion of the cycle. This trace is considered representative of the operating condition, as it corresponds to an actual measured in-cylinder pressure profile as opposed to that of the ensemble-averaged trace. With the selected pressure trace, then the apparent rate of heat release is determined through a validated GT-Power engine model. In this study, GT-Power was used to construct a single-cylinder engine model reflecting the experimental test bench configuration. Combustion analysis was conducted using both non-predictive and predictive approaches. The non-predictive method relies on a reverse-run simulation based on a two-zone thermodynamic combustion model, which partitions the cylinder volume into unburned and burned zones. Using measured in-cylinder pressure as input, the reverse simulation iteratively solves energy conservation equations to deduce the apparent burn rate, enabling heat release characterization without the need for detailed chemical kinetics or flow field data. Calculations of efficiency and the heat release rate, which are critical for subsequent discussions, are briefly summarized here. The net indicated efficiency (η_i) is a parameter used to evaluate the efficiency of the full engine cycle, and it is calculated by the ratio of IMEP and fuelMEP [32]. Equation (3) describes the heat release calculation, with γ the ratio of specific heats, p the instantaneous pressure at a particular CAD and wall heat losses, ($dQ_w/d\theta$) in J/CAD, calculated using Woschni's correlation [32].

$$\frac{dQ}{d\theta} = \frac{\gamma}{\gamma - 1} \cdot p \cdot \frac{dV}{d\theta} + \frac{1}{\gamma - 1} \cdot V \cdot \frac{dp}{d\theta} + \frac{dQ_w}{d\theta} \tag{3}$$

The cumulative heat release, which is the integral of the gross heat release rate, should equal the total energy content of the injected fuel during the cycle. However, this is only true in the ideal case where the amount of unburned fuel is zero. In this study, the unburned fuel content in the exhaust was not directly measured, and the wall temperature, needed to calculate heat losses, was estimated from a temperature probe located near the cylinder wall. Even though the individual contributions of these losses are uncertain, their combined effect should equal the difference between the total fuel energy and the sum of the work and the internal energy contributions. This is represented as 'Losses' in Figure 3. In order to ensure that the cycle energy is balanced, GT-Power allows for modification of the overall convection multiplier to increase or reduce the wall heat losses, and the unburned fuel quantity can be specified. For all operating conditions investigated, the overall convection multiplier was left as unity (i.e. calculation of wall heat loss directly from the Woschni's correlation and estimation of wall temperatures measured from the thermocouples on the engine body), with the remainder of losses attributed to unburned fuel for energy closure. This resulted in excellent agreement with the expected energy balance. While there is no accurate distinction between these sources of loss, there is also no appreciable impact on the generality of the results shown in later sections, as discussion is focused on the distribution of useful work and internal energy of the combustion chamber contents with no particular requirement to distinguish between sources of loss. Using the pre-processed median pressure trace, a validated 0D - 1D GT-Power combustion model of the engine cylinder is used in a reverse-run mode to solve for the apparent rate of heat release as described in Equation 3, ensuring there is conservation of energy during the engine cycle and matching the experimental pressure trace. The model was first calibrated with a motoring pressure trace. This provided a basis to verify the reverse run simulation using data under oxy-CH_4 SI conditions at 1500 RPM. Figure 2 shows the close agreement of the measured pressure trace and the pressure trace generated from the reverse-run simulation for a set of operating condition (Sl. No. 1-10). From the fully processed engine cycle, one of the key derived quantities later utilized in Section 5 is determined; the coefficient of variation (CoV) of indicated mean effective pressure (IMEP):

$$CoV_{\mathrm{IMEP}} = \frac{100}{\overline{\mathrm{IMEP}}} \cdot \sqrt{\frac{1}{N} \cdot \sum_{i=1}^{N} (\mathrm{IMEP}_i - \overline{\mathrm{IMEP}})^2} \tag{4}$$

In Equation (4), IMEP_i denotes the IMEP of the i^{th} cycle within an ensemble of $N = 100$ cycles, while $\overline{\mathrm{IMEP}}$ represents the av-

erage IMEP. To verify that analyzing 100 cycles provides statistically significant results, the coefficient of variation of IMEP, CoV_{IMEP}, was examined as a function of the number of cycles included in the averaging. It was found that beyond 60 cycles, CoV_{IMEP} approached an asymptotic value even under the most unstable operating conditions, justifying the selection of 100 cycles for the analysis. This parameter is often used as an indication of combustion instability, as a higher value represents more cycle-to-cycle variability that approaches the instability limit at which bulk flame quenching and misfire occurs (5% is considered as the threshold in literature [32]).

3.3. Determining the engine operation regime with non-dimensional analysis

Once the GT-Power reverse-run engine model is validated at a given experimental operating condition, the premixed turbulent combustion model is employed to provide further insight into the combustion regime and its relationship to bulk flame quenching and the instability limit. These regimes are defined by several key non-dimensional numbers that can be determined by extracting derived quantities from the GT-Power simulation, the first of which is the Damköhler number, Da:

$$Da = \frac{\tau_{flow}}{\tau_{chemical}} = \frac{\frac{L_T}{u_k^t}}{\frac{\delta_L}{S_L}} = \frac{L_T}{u_k^t} \cdot \frac{S_L}{\delta_L} \tag{5}$$

The Damköhler number is defined as the ratio between the flow timescale (τ_{flow}) and the chemical timescale ($\tau_{chemical}$). In this equation, L_T is the turbulent length scale, u_k^t is the turbulent intensity, both of which are extracted from the turbulent combustion simulation. S_L is the laminar flame speed, whose calculation procedure by Cantera (an open source software to resolve chemical kinetics, thermodynamics and transport process in a reacting system) is described in detail in Section 3.4.1, and δ_L is the laminar flame thickness which is defined as:

$$\delta_L = \frac{\mu}{\rho \cdot S_L} \tag{6}$$

where μ is the dynamic viscosity and ρ is the density. In this study μ, ρ, u_k^t and L_T are determined from the GT-Power software. The second key non-dimensional parameter used to determine the combustion regime of a reciprocating engine is the turbulent Reynolds number, Re_T, which can be written in terms of the same quantities as Da:

$$Re_T = \frac{u_k^t \cdot L_T \cdot \rho}{\mu} = \frac{u_k^t}{S_L} \cdot \frac{L_T}{\delta_L} \tag{7}$$

These non-dimensional quantities will be utilized in Section 5 for the identification of the engine operating regime under oxy-fuel combustion compared with that of conventional air-combustion. Such visual guides are instructive to qualitatively assess how CO_2-diluted oxy-fuel operation deviates from that of standard premixed reciprocating engines.

3.4. Characterizing the instability limit using the theory of premixed turbulent combustion

Bradley et al. [29, 30] examined how turbulent strain influences flame stretch and quenching near the lean instability limit. Their work essentially quantified the balance between turbulence enhancing the mixing of unburned fuel-air mixtures into the reaction zone and turbulence inducing excessive flame stretch that ultimately resulted in flame extinction. Abdel Gayed et al. [33, 34] proposed a correlation encompassing all the experimental data available at that time for turbulent burning velocities over a broad range of equivalence ratios, covering methane, propane, iso-octane, and hydrogen-air mixtures. This correlation employs dimensionless quantities that describe the competing effects due to turbulence, including the Karlovitz stretch factor (K) [33, 34]:

$$K = \frac{u_k^t}{l_T} \cdot \frac{\delta_L}{S_L} \quad with \quad l_T = \frac{C_{TLS} \cdot L_T}{\sqrt{Re_T}} \tag{8}$$

K is used to represent the impact of turbulence on a flame, as it describes the factor by which the flame is stretched due to turbulence in comparison with the propagation of an unstretched, laminar flame. Therefore, it was surmised that this quantity relates to the instability limit due to flame extinction from excessive stretch due to turbulence. From the GT-Power turbulent combustion simulation, K is determined using Equation 8, where l_T is the Taylor microscale of turbulence and C_{TLS} is the Taylor length scale multiplier. This represents a tuning factor to adjust the estimated eddy size or eddy turnover time to better match with the actual engine operation. Following from equation 8, K can be calculated:

$$\begin{aligned} K &= \frac{1}{C_{TLS}} \cdot \left(\frac{u_k^t}{S_L}\right)^2 \cdot \frac{1}{\sqrt{Re_T}} \\ &= \frac{1}{C_{TLS}} \cdot \left(\frac{u_k^t}{S_L}\right)^{1.5} \cdot \left(\frac{\delta_L}{L_T}\right)^{0.5} \\ &= \frac{1}{C_{TLS}} \cdot \frac{{u_k^t}^{1.5}}{S_L^2} \cdot \left(\frac{\mu}{\rho \cdot L_T}\right)^{0.5} \end{aligned} \tag{9}$$

Additionally, Abdel Gayed et al. [35, 36] studied how the effects of strain interact with molecular thermal-diffusive processes, represented by the Lewis number (Le) of the original reactants. Le, which is the ratio of the thermal diffusivity (α) to the mass diffusivity (Equation 10), represents the heat diffused from the flame in comparison to the diffusion of unburned fuel-air mixture into the flame, and is therefore connected to the notion of flame stability. It was concluded that higher Le values lead to a greater influence of flame straining, and therefore tend to move the flame towards the bulk quenching regime.

$$Le = \frac{\alpha}{D_{ij}} = \frac{k_t}{\rho \cdot c_p \cdot D_{ij}} \tag{10}$$

Le can be directly evaluated with k_t and D_{ij}, representing the mixture thermal conductivity and the mass diffusion coefficient, respectively. In this work, the thermal diffusivity and mass diffusivity are extracted from Cantera, based on the mixture composition, temperature, and pressure corresponding to a specific

operating condition. Abdel Gayed et al. [36] ultimately determined that a flame quenching criterion could be developed from the product $K\,Le$. The so-called 'Bradley diagram', illustrates these quenching conditions in various regions, alongside empirically derived curves for $K\,Le$ and $Re_T \cdot Le^{-2}$. The physical interpretation of this diagram is intricately connected with the instability limit of combustion; higher values of $K\,Le$ indicate increasing proclivity for bulk flame quenching due to the dominating effect of turbulent flame stretch over turbulent entrainment of unburned fuel-oxidizer mixture. In this work S_L is obtained from chemical kinetics simulations using Cantera, while S_T and u_k^t are extracted from the predictive turbulent combustion model implemented in GT-Power. The $K\,Le$ values for different operating conditions can be calculated using Equation 9 and 10, utilizing parameters extracted from the predictive model, specifically, S_L and u_k^t. In subsequent sections, these values will first be evaluated against experimental measurements of combustion stability, such as $\mathrm{CoV_{IMEP}}$. This comparison aims to evaluate the effectiveness of turbulent premixed combustion theory in predicting instability over a range of reactant Le and oxidizer mixtures. Bradley et al. [29] further characterized turbulent flame propagation regimes by analyzing schlieren films at various $K\,Le$ values and compared their observations with those initially proposed by Borghi [37]. By plotting (u_k^t/S_L) against (L_T/δ_L) on a logarithmic scale, constant values of K and Re_T are represented as straight lines on the Borghi diagram, as expressed in Equations 7 and 9. Figure 6 delineates the boundaries of different combustion regimes with the corresponding K values, as originally suggested by Borghi [37]. The diagram integrates the updated terminology introduced by Peters [38], with Borghi's original nomenclature included in parentheses. The validity of the flamelet assumption in turbulent premixed combustion, which assumes that burning takes place at thin flame surfaces, has recently been reevaluated by Sina et al. [39]. Their findings indicate that both the preheat and reaction zones of the flame may undergo significant thickening with increasing turbulence intensity. This thickening is primarily attributed to the intrusion of turbulent eddies into the flame structure, which not only alters the physical thickness of the flame but also influences the turbulent flame combustion chemistry. Specifically, deviations from the laminar flame chemistry have been observed and quantified, a phenomenon commonly referred to in the literature as non-flamelet behavior. Sina et al. [39] utilized the non-dimensional Karlovitz number, Ka, to characterize the combustion regimes. It is defined as the ratio between the chemical time scale ($\tau_{chemical}$) and the Kolmogorov time scale (τ_η), the latter being the ratio between the Kolmogorov microscale (η) and the Kolmogorov velocity scale (u_η) [40, 39]. Ka describes the degree to which the smallest eddies affect the flame, and can be evaluated in terms of the turbulent intensity, S_L and Re_T:

$$Ka = \frac{\tau_{chemical}}{\tau_\eta} = \frac{{u_k^t}^2}{{S_L}^2} \cdot \frac{1}{\sqrt{Re_T}} = C_{TLS} \cdot K \qquad (11)$$

For $Ka < 1$, the flame thickness is less than the smallest scale turbulence, and therefore turbulence does not impact the flame's burning velocity (corresponding to flamelets), while $Ka > 1$ indicates that the turbulence field is able to enter and influence the preheat zone of the premixed flame, or at high enough values, enter the reaction zone. To continue, Borghi's first hypothesis states that flame surfaces can be indefinitely wrinkled by increasing turbulence intensity, leading to a continuous rise in the turbulent flame consumption speed. This concept is typically visualized as a linear relationship when the turbulent flame speed normalized by the laminar flame speed (S_T/S_L) is plotted against the normalized turbulent intensity (u_k^t/S_L), similar to the Bradley diagram. However, this linear trend has been refuted by experimental observation. Experimental measurements show a clear deviation from linearity, characterized by a bending of the curve toward the horizontal axis as turbulence intensity increases, indicating a saturation and eventual reduction in S_T. Ref. [40] critically examined the divergence between the predictions of Borghi's hypothesis and empirical data. It was found that while the turbulent flame speed initially increases with rising turbulence intensity, it eventually plateaus and declines as the flame front becomes increasingly distorted and susceptible to local quenching. Physically, the Damköhler number serves as an indicator of flame stability under turbulent conditions; lower values of Da imply greater flame sensitivity to turbulence and a higher risk of quenching. In conclusion, this work seeks to evaluate the broader applicability of premixed turbulent combustion theory to describe oxy-fuel combustion and its instability limit. This is accomplished by employing the aforementioned non-dimensional analysis, including the Damköhler number (Da), Karlovitz number (Ka), and Karlovitz stretch factor (K), determined through reduced-order modeling and compared to experimental measurements of instability (i.e. $\mathrm{CoV_{IMEP}}$).

3.4.1. Prediction of laminar flame speed using Cantera

In order to use the predictive turbulent combustion model in GT-Power, it is crucial to provide an appropriate correlation for S_L, as this parameter plays a fundamental role in governing the combustion process. However, GT-Power does not include a built-in correlation for oxy-fuel combustion. To address this limitation, a lookup table was developed using a comprehensive dataset of S_L values calculated with Cantera. For the first experimental campaign, the dataset was generated using the GRI Mech 3.0 mechanism. This mechanism was tested for oxy-CH_4 combustion and compared against S_L values calculated with Aramco Mech 3.0. The comparison demonstrated strong agreement, confirming the reliability of GRI Mech 3.0 for modeling oxy-methane combustion [41, 42]. For the second experimental campaign, which involved fuel mixtures of CH_4 and H_2, including potentially high H_2 fractions, a different mechanism was required. Changwei et al. [43] evaluated several chemical mechanisms against experimental data available in the literature to identify the most suitable option. Based on their findings, the San Diego Mech mechanism was determined to be well-suited for the operating conditions of the second experimental campaign. Consequently, this mechanism was selected to construct the dataset for oxy-CH_4/H_2 combustion. To validate this choice, both datasets were implemented in the predictive GT-

Power model (which will be further explained in subsequent sections) to simulate the baseline operating condition of 36% O_2 for oxy-CH_4 combustion. The results confirmed that both datasets were interchangeable within the GT-Power model, further supporting the fidelity of the selected mechanisms.

3.4.2. GT-Power predictive combustion modeling

The predictive modeling approach in GT-Power employs the Spark-Ignition Turbulent Flame Model (EngCylCombSITurb), which computes combustion evolution based on in-cylinder thermodynamic and flow conditions. In the preceding period of this study, CFD simulations were performed to determine turbulent conditions, namely, swirl number, tumble number, turbulent length scale and turbulent intensity. The values of these parameters at IVC are used as an input in the GT-Power software. This single cylinder model incorporates laminar and turbulent flame speed formulations, influenced by equivalence ratio, residual gas fraction, and turbulence intensity. Calibration of model constants, such as the Taylor microscale and flame kernel growth factors, is essential to reconcile predicted burn rates with experimental observations. Together, these methods provide a robust framework for simulating and analyzing combustion in spark-ignition engines under varying fuel compositions and dilution strategies. As previously mentioned, the experimental data was used to validate the reverse run simulations and these were in turn used to develop the predictive turbulent combustion model. Equation 12 shows the normalized root mean square error (NRMSE) of pressure for the comparison between simulated and measured in-cylinder pressure.

$$NRMSE = \sqrt{\frac{1}{N} \cdot \sum_{i=1}^{N} \left(\frac{p_{sim}(i) - p_{meas}(i)}{p_{meas}(i)} \right)^2} \qquad (12)$$

where p_{meas} and p_{sim} denote the in-cylinder pressures obtained from measurements and simulations over the crank angle, respectively, and N represents the total number of crank angle samples. A threshold of 5% for the NRMSE was selected as the convergence criterion for the simulations, consistent with criteria established in previous studies [44]. Table 4 presents the NRMSE values for both the reverse run (RR) and the predictive model (PR). Calibration of the turbulent flame speed is performed using GT-Power's built-in optimization tool to closely match the $\frac{dQ}{d\theta}$ profiles from the predictive model and reverse run simulations. This calibration involves tuning the Taylor Length Scale Multiplier (C_{TLS}), Turbulent Flame Speed Multiplier (C_{TFS}), and Flame Kernel Growth Multiplier (C_{FKG}). The calibrated values for the examined operating conditions are summarized in Table 4. Figure 2 provides a graphical comparison of the measured, reverse run, and predicted crank-angle resolved in-cylinder pressures, illustrating the close agreement between the predictive model and the experimental data. All parameters required to determine the non-dimensional quantities for the turbulent premixed combustion theory in section 3.3 and 3.4 are are data obtained by GT-Power.

Table 4: Calibration constants used in the predictive GT-power model.

Sl.No.	RR	PR	C_{TLS}	C_{TFS}	C_{FKG}
1	0.019	0.018	3.064	0.374	6.777
2	0.014	0.023	2.325	0.357	3.943
3	0.010	0.016	3.110	0.383	6.354
4	0.011	0.015	4.907	0.561	6.729
5	0.010	0.013	7.081	0.705	5.753
6	0.010	0.016	3.110	0.383	6.354
7	0.006	0.015	3.733	0.508	10.160
8	0.009	0.017	4.651	0.741	12.885
9	0.012	0.012	6.729	0.818	5.825
10	0.015	0.015	9.415	1.159	11.824

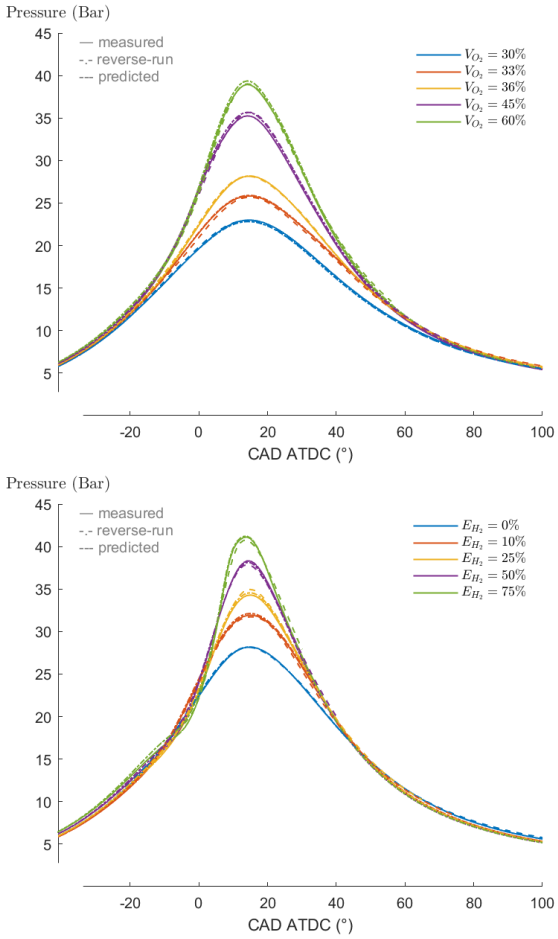

Figure 2: Measured, reverse run and predicted in-cylinder pressures for varying oxygen concentrations with pure methane-fueling and varying hydrogen concentration with fixed oxidizer composition of 36% O_2 and 64% CO_2.

4. The impact of CO_2-diluted oxidizer and fuel composition on engine output

The analysis of the experimental results begins with the identification of a potential use-case for this combustion concept in reciprocating engines; CO_2-diluted oxy-fuel combustion in the context of stationary power and heat generation. Utilizing the heat release analysis with the experimentally-measured pressure trace and single-cylinder combustion model, a cyclic energy balance for each operating condition is calculated showing the distribution between useful work, internal energy of the

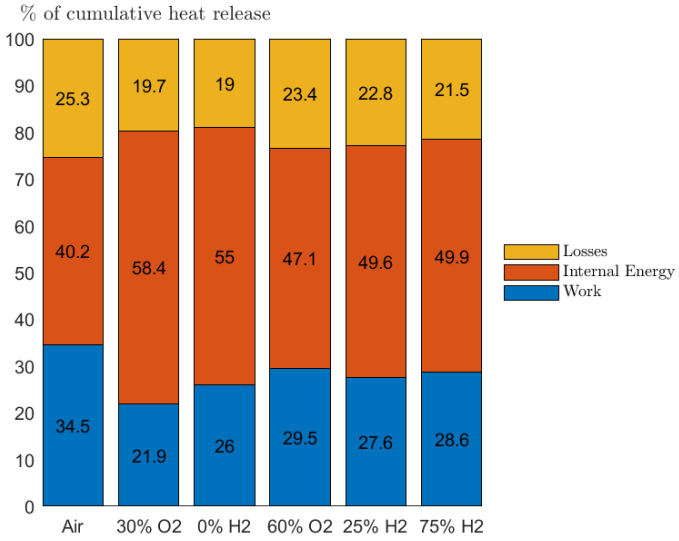

Figure 3: Work, internal energy of chamber contents and unburned fuel/wall heat losses as percentages of the overall injected chemical energy for the following combustion cases from left to right, based on the operating conditions (OC) presented in Table 3 stoichiometric CH_4-air, OC 1, OC 6, OC 5, OC 8 and OC 10.

chamber gases and the combination of losses via heat transfer to the wall and any unreacted fuel. The apparent rate of heat release, as determined by Equation 3, is used to calculate the cumulative contributions of the injected chemical energy over the thermodynamic engine cycle, under the given operating conditions as depicted in Figure 3. The shift in internal energy and work observed when comparing oxidizer mixtures containing 30% and 60% O_2 can be explained by two key mechanisms. The first mechanism is related to the influence of the specific heat ratio (γ) of the mixture. CO_2 exhibits a higher specific heat capacity (c_p) and a lower specific heat capacity ratio (γ) compared to O_2. Consequently, the impact of CO_2-dilution is primarily thermal, as it serves as a more effective heat sink in the combustion chamber than diatomic species. The thermal effect leads to a reduction in temperature (and consequently pressure) during combustion. However, due to the reduced thermal quenching effect resulting from decreased CO_2 levels, higher temperatures and pressures are achieved within the combustion chamber. Consequently, a greater proportion of the fuel's released heat is converted into mechanical work, while the internal energy of the chamber gasses is reduced. The chemical quenching effect of CO_2 found in engines that use exhaust gas recirculation (EGR) is less relevant here, as the operating conditions of this study generally involve oxygen concentrations enriched above levels found in air. The second mechanism governing the redistribution of internal energy and work is the reduction in combustion duration, calculated from cumulative heat release rate, with increasing O_2 concentration. This shift makes the combustion process more isochoric, thereby increasing the proportion of fuel chemical energy converted into useful mechanical work rather than raising the internal energy of the combustion products. Continuing with the evaluation of H_2 concentration in the fuel mixture, an increase of H_2 concentration in the fuel mixture lowers the overall oxidizer concentration in the mixture, and therefore reduced thermal quenching from the CO_2-diluted oxidizer. Although, the reduction of combustion duration plays a more dominant role in the redistribution of internal energy and work. Higher H_2 content accelerates combustion, and in comparison to O_2 enrichment in the oxidizer, the H_2 addition has a more pronounced impact on decreasing burn duration. In conclusion, combustion performance improves due to the mechanisms discussed. Although the useful work shows an overall increase, compared to stoichiometric CH_4-air combustion with the same mixture strength, it remains significantly lower. As illustrated in Figure 3, this underscores the dominant influence of CO_2 presence within the combustion chamber. The thermal quenching effect of the oxy-fuel oxidizer mixture reduces the in-cylinder temperature. This leads to a lower temperature gradient between the hot gases and the chamber walls, thereby reducing heat dissipation through the walls, which is directly connected to the reduction in losses shown in Figure 3. This suggests that CO_2-diluted oxy-fuel combustion is most suitable for combined heat and power (CHP) applications. The resulting higher enthalpy of the high-temperature exhaust gases could be effectively utilized in such systems to compensate for the reduction in mechanical work when transitioning from conventional air combustion to CO_2-diluted oxy-fuel combustion, while also providing the added advantage of eliminating NO_x emissions. Such zero-NOx CHP units could have improved overall efficiency in comparison with air-combustion equivalents, with efficiency gains ranging from 1.9% (OC5) up to 6.3% (OC3) relative to CH_4-air combustion, as shown in Figure 3.

5. Prediction of generalized instability limit for a range of oxidizer and fuel mixtures using premixed turbulent combustion theory

While the overall performance of oxy-CH_4/H_2 mixtures is now established, a generalized understanding of the dilution limits of such reciprocating engines is still unresolved. The successful implementation of zero-NO_x, oxy-fuel CHP units, as previously discussed, requires a comprehensive understanding of the operability limits of such engine platforms. Therefore, this section aims to provide a generalized characterization of these operating limits based on the fundamental principles of premixed, turbulent combustion. Given its ubiquitous presence in many of the trends observed in the experimental results, this discussion begins with a detailed assessment of the laminar flame speed under the tested conditions. Using the predictive model from GT-Power, the effects of variations in both oxidizer composition and fuel mixture on laminar and turbulent flame speeds are analyzed. The variation of S_L is presented as a function of crank angle degree (CAD) in Figure 4. Additionally, combustion loci are visualized alongside five specific mass fraction burned (MFB) markers: CA2, CA10, CA50, CA90, and the end of combustion (EOC, CA99). The laminar and turbulent flame speeds increase with higher O_2 concentrations in the oxidizer mixture as well as with greater H_2 content in the fuel mixture. The influence of CO_2 dilution in oxy-fuel combustion is further illustrated in the combustion regime diagram in Figure

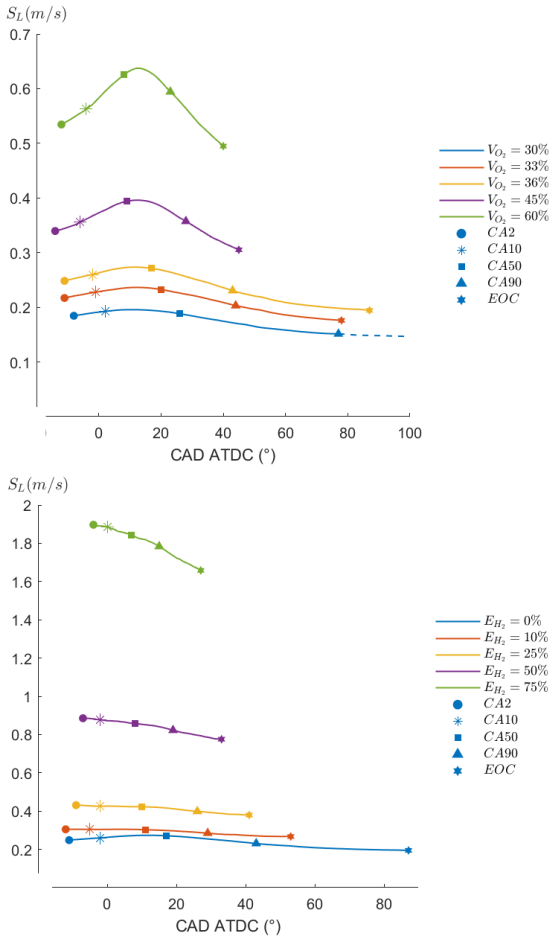

Figure 4: S_L for varying oxygen concentrations and varying hydrogen concentration.

5, which classifies combustion modes based on the Damköhler number (Da) and the turbulent Reynolds number (Re_T). The combustion loci at CA90 are depicted, where the ratio S_T/S_L reaches its maximum, following the methodology outlined in [45]. The combustion regimes are categorized as follows: weak turbulence, where $u_k'/S_L < 10^{-2}$; reaction sheets, where the Kolmogorov microscale (η) exceeds the flame thickness (δ_L); and distributed reactions, where the turbulent length scale (L_T) is smaller than (δ_L) [45]. Most data points fall below the $\eta = \delta_L$ boundary. As the O_2 or H_2 concentration increases, these points shift closer to this boundary, emphasizing the critical role of laminar flame speed in defining the combustion regime in oxy-fuel engines. An increase in O_2 or H_2 concentration (along with an increase in λ' in case of O_2) leads to higher laminar flame speeds, thereby shortening the chemical timescale (δ_L/S_L) and increasing Da. As a result, the operating regime of the CO_2-diluted oxy-fuel engine gradually transitions toward the combustion characteristics typical of conventional engines, as indicated by the shaded "Engine Regime" region in Figure 5. Figure 6 presents the combustion regimes proposed by Borghi [37], characterized in terms of u_k'/S_L and L_T/δ_L, along with key timescales: the flow timescale ($\tau_{flow} = \tau_L$), Kolmogorov timescale (τ_η) and chemical timescale ($\tau_{chemical} = \tau_c$). The combustion loci at CA90, where S_T/S_L reaches its maximum, are depicted for both increasing O_2 concentration in the oxidizer

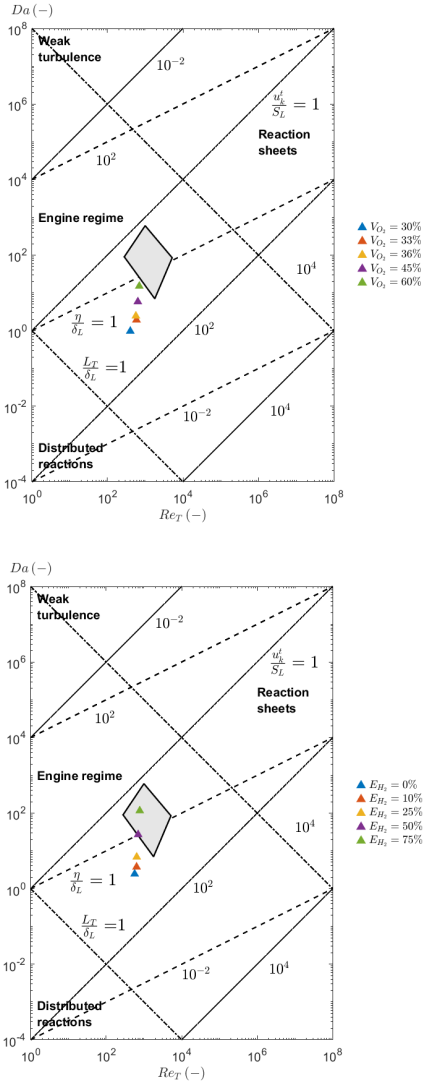

Figure 5: The combustion regimes as a function of Da and Re_T, proposed by Heywood [32], for varying oxygen concentrations and hydrogen concentrations listed in Table 3 as OC1-OC5 (top) and OC6-OC10 (bottom).

mixture and increasing H_2 concentration in the fuel mixture. It is important to note that this diagram does not account for Lewis number (Le) effects. As shown in Figure 6, for oxy-CH_4 combustion, the combustion regime predominantly falls within the thickened-wrinkled flame regime, outside the typical flamelet regime of air-combustion engines. At higher O_2 concentrations, the operating point shifts further towards the corrugated flamelet regime, where the flame thickness becomes smaller than the Kolmogorov microscale ($\delta_L < \eta$). This transition moves the operation away from the thickened-wrinkled flame regime, where η becomes less than δ_L, indicating that the smallest turbulent eddies can perturb the flame structure and potentially cause extinction. The increase in laminar flame speed due to elevated O_2 concentration causes the combustion locus to shift downward and to the right, as flame thickness (δ_L) is inversely proportional to S_L. A similar trend is observed in oxy-fuel combustion with H_2-CH_4 mixtures. At the highest H_2 concentrations, the combustion regime moves even further into

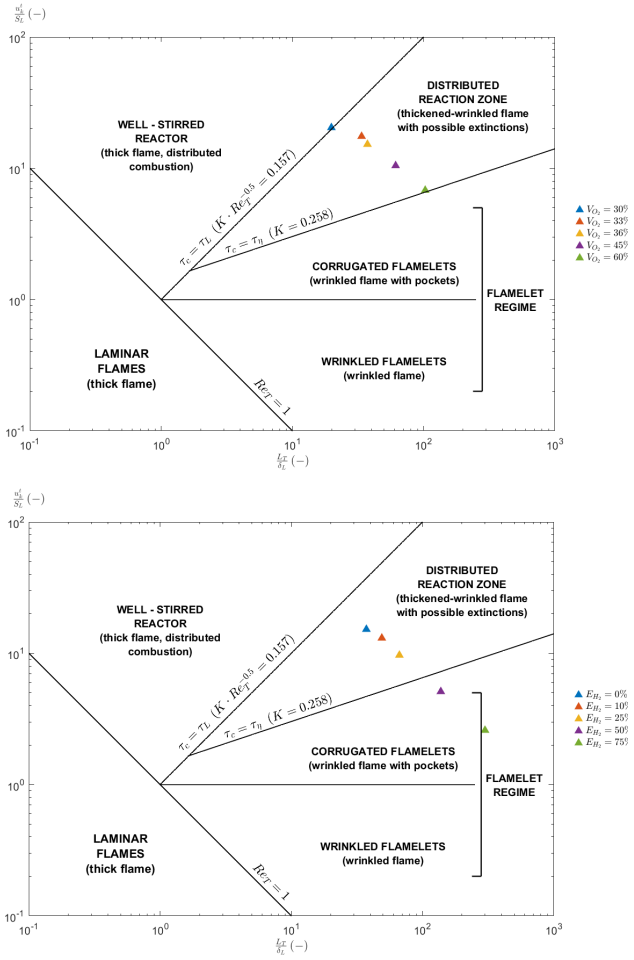

Figure 6: The combustion regimes proposed by Borghi [37, 29] for varying oxygen concentrations and hydrogen concentrations listed in Table 3 as OC1-OC5 (top) and OC6-OC10 (bottom).

the corrugated flamelet regime, reinforcing the dominant influence of H_2 on combustion characteristics. These shifts provides insight into the experimentally observed combustion stability, an increase in laminar flame speed results in a downward and rightward shift of the combustion locus, further highlighting the critical role of flame speed in determining combustion stability. $K\,Le$ is derived from Equation 9 using the Le from Equation 10. Table 5 displays the calculated Le for the different MFB points for both increasing O_2 concentration in the oxidizer mixture and increasing H_2 concentration in the fuel mixture. It is seen that the Le remains nearly constant throughout the combustion process, and for the calculation of $K\,Le$ values, a constant Le at CA2 is used. In the past these quantities have been used in the so-called Bradley diagram. While this approach has been used to provide some qualitative insight into the instability limit [45], directly evaluating K from Equation 9 and plotting it on the Bradley diagram is of questionable validity for this reduced-order analysis of turbulent combustion in spark ignition (SI) engines. The Bradley diagram is constructed empirically from experiments involving explosions in fan-stirred bombs and burners [33, 34, 35, 36, 46], which assumes isotropic turbulence, a condition not present in the combustion chamber of the engine used in this research, and not typically expected in reciprocating engines. For this reason, the relationship between turbulent and laminar flame speed diverges as turbulence increasingly affects the flame structure, placing the combustion locus in regimes that fall outside the valid scope of the Bradley diagram. Instead, the theoretically predicted $K\,Le$ values, which indicate a propensity for bulk flame quenching and thus theoretically inferred combustion instability, are compared to experimentally measured combustion instability using CoV_{IMEP} at CA2 for both increasing O_2 concentration in the oxidizer mixture and increasing H_2 concentration in the fuel mixture. The $K\,Le$ predictions are particularly relevant at lower MFB locations, where the flame is more susceptible to quenching during the initial combustion stages [32, 47]. The results show that the linear approximations for both experimental campaigns exhibit distinct slopes. The R^2 values indicate that the $K\,Le$ values directly evaluated from Equation 9 exhibit a stronger correlation with CoV_{IMEP} compared to those interpreted from the Bradley diagram. This indicates the presence of a trend within each dataset, however, it also demonstrates that a direct generalization across the different experimental campaigns is not obvious. In order to find a more general, unifying relationship between measured and theoretically predicted instability, the non-dimensional quantity $K\,Le$ is first considered. It is important to note that the C_{TLS} parameter (a tuneable Taylor length scale multiplier in GT-Power) has an influence on the value of K. Given that C_{TLS} lacks a direct physical interpretation related to combustion processes, it suggests that a more general choice of instability prediction may arise from the product of Ka and Le rather than K and Le. K is related to Ka based on Equation 11 [48]. As previously demonstrated, the value of Ka is deeply connected with the flame regime and the quenching limit, and it is adopted for the following analysis in place of K. While Ka still depends on quantities calculated by the predictive, turbulent combustion model in GT-Power, it avoids the inclusion of a tuning constant, and therefore is expected to enhance the physical relevance of the proposed correlation. To this end, Figure 7 presents the CoV_{IMEP} values plotted against the $Ka\,Le$ parameter for three experimental campaigns. The first two campaigns correspond to those discussed earlier, while the third includes additional data obtained from previous experimental investigations. When all operating conditions from the various experimental campaigns are combined into a single plot, a clear trend emerges. An exponential regression function is fitted to the combined dataset, along with its corresponding R^2 value, as shown in Figure 7. The strong agreement between

Table 5: Le in function of MFB locations for varying oxygen concentrations and varying hydrogen concentration.

Sl. No.	CA2	CA5	CA10	CA50	CA90
1	0.808	0.808	0.807	0.804	0.803
2	0.813	0.813	0.813	0.808	0.807
3	0.819	0.818	0.817	0.812	0.811
4	0.836	0.836	0.834	0.826	0.824
5	0.867	0.865	0.863	0.852	0.849
6	0.819	0.818	0.817	0.812	0.811
7	0.566	0.565	0.564	0.560	0.599
8	0.645	0.643	0.640	0.632	0.632
9	0.565	0.562	0.560	0.554	0.555
10	0.525	0.523	0.521	0.517	0.519

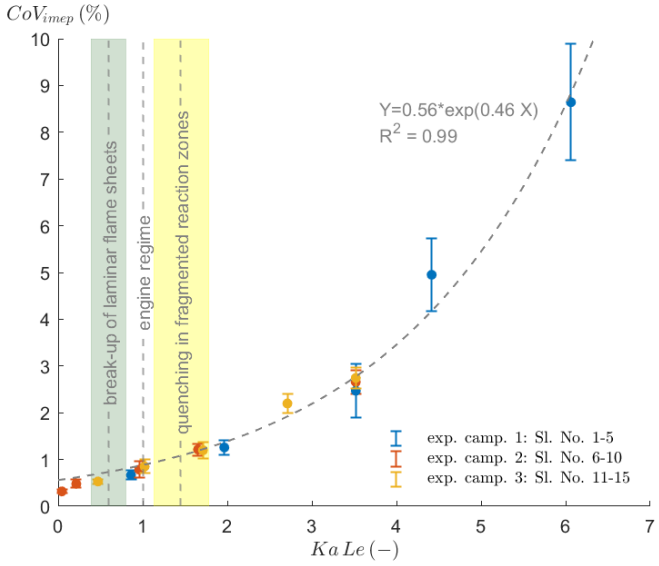

Figure 7: CoV_{imep} as a function of $Ka\,Le$, calculated from Equation11, for three experimental campaigns listed in Table3 as OC1–OC5 (blue), OC6–OC10 (red), and OC11–OC15 (yellow).

the regression model and the experimental data suggests that premixed turbulent combustion theory can capture trends in the experimentally measured instability limits across a wide range of oxidizer and fuel compositions in oxy-fuel combustion systems. A final note regarding Figure 7 is the non-linear shape of the correlation between CoV_{IMEP} and $Ka\,Le$. The operating condition with the highest value of $Ka\,Le$ is a condition with pure methane, and oxidizer consisting of 30% O_2 and 70% CO_2 (SI. No. 1 in Table 3). This is a condition of low laminar flame speed (below 20 cm/s), and as indicated in the Borghi diagram, lies far outside the flamelet zone. In fact, the regime diagram suggests that this condition departs appreciably from typical SI flame propagation, and may contain localized zones where there is flame quenching, and those where there is the reaction of a highly thickened flame, made possible through the oxygen-enriched environment compared to that of air. In contrast to overall exponential correlation, a simple, linear function is sufficient to describe the relationship between $Ka\,Le$ and $\mathrm{CoV}_{\mathrm{IMEP}}$ at lower values of $Ka\,Le$ (i.e. $Ka\,Le <= 1$), corresponding to cases where the combustion is closer to the wrinkled flames regime. This seems to indicate that within the flamelet regime, the predicted instability through reduced-order modeling relates to experimentally measured instability in a straightforward manner over a range of fuel and oxidizer mixtures. Outside this regime, the theoretically predicted instability by $Ka\,Le$ still correlates strongly with experimental instability, though higher-order effects are now present, potentially in the form of interactions between the turbulence field and the flame in thickened reaction zones. Such effects cannot be resolved in a direct way through the simple 0D combustion model used in this study. It is proposed that future work encompasses a detailed 3D CFD of the engine cycle to determine if there is indeed localized flame quenching and distributed reaction through the cylinder during the combustion event in cases of extreme reaction zone thickening and low laminar flame speeds.

6. Conclusions

This study presented a combined numerical and experimental investigation of CO_2-diluted oxy-CH_4/H_2 combustion in a reciprocating engine. Two targeted experimental campaigns were carried out, both originating from a baseline CO_2-diluted oxy-CH_4 condition. Experiments confirmed that the high density and low thermal diffusivity of CO_2 impeded flame propagation, leading to slower combustion and decreasing the proportion of the useful work for the engine cycle. Increasing O_2 enhanced mixture reactivity and flame speed, while the addition of H_2, with its inherently high laminar flame speed, rapidly accelerated combustion. Notably, oxy-fuel combustion can mitigate H_2's high reactivity, as CO_2 acts as a pre-ignition suppressant, enabling high fMEP operation with hydrogen and hydrogen-enriched fuel blends. Moreover, CoV_{IMEP} decreased substantially with higher O_2 and H_2 concentrations, indicating improved combustion stability. An energy balance analysis revealed that the distribution of energy for the CO_2-diluted oxy-fuel operating conditions tended to have proportionally lower total losses, shifting relatively more of the energy share to the internal energy of the chamber gases. These findings suggested that combined heat and power (CHP) applications are promising for CO_2-diluted oxy-CH_4/H_2 engines, as exhaust heat recovery can offset the lower fuel conversion efficiency, with the added benefit of zero-NO_x output. Combustion instability limits were further explored using predictive modeling to determine key non-dimensional quantities to compare theoretical predictions against experimentally measured instability. Although the original theory was developed for air-diluted systems, it was extended to include generalized fuel and oxidizer blends comprising CH_4, H_2, O_2, N_2, and CO_2. The results show a strong correlation between the directly evaluated Ka, Le quantity and experimentally observed instability, defined by CoV_{IMEP}, particularly when the flamelet assumption holds at low Ka, Le values. As Ka, Le increases and combustion transitions from the flamelet regime toward distributed reaction zones or quenching, this relationship becomes exponential. This suggests the presence of higher-order effects, highlighting the need for further investigation into complex turbulence-chemistry interactions in highly diluted oxy-fuel combustion flames that appear to feature thickened reaction zones.

Declaration of generative AI and AI-assisted technologies in the writing process

During the preparation of this work the author(s) used ChatGPT in order to improve the readability and language of the manuscript. After using this tool/service, the author(s) reviewed and edited the content as needed and take(s) full responsibility for the content of the publication.

CrediT authorship contribution statement

Daese Mauro: Writing - original draft, Investigation, Methodology, Formal analysis. **Josh Lacey**: Writing - review & editing, Methodology, Investigation. **Francesco Contino**: Writing - review & editing, Methodology, Investigation, Resources.

Declaration of competing interest

The authors declare that they have no known competing financial interests or personal relationships that could have appeared to influence the work reported in this paper.

Acknowledgments

This work was supported partly through the Energy Transition Funds of the FPS Economy (A21/TT/1994) and VLAIO Moonshot funding (HBC.2021.0589).

References

[1] C. Fetting, The european green deal, ESDN report, December 2 (9) (2020) 53.

[2] Z. Yue, X. Wang, H. Liu, B. Li, M. Yao, Exploring the application of oxy-fuel combustion to methanol spark ignition engines, Applied Energy 367 (2024) 123449.

[3] K. Senecal, F. Leach, Racing toward zero: the untold story of driving green, SAE International, 2021.

[4] A. Franco, C. Giovannini, Recent and future advances in water electrolysis for green hydrogen generation: Critical analysis and perspectives, Sustainability 15 (24) (2023) 16917.

[5] S. Talei, D. Fozer, P. S. Varbanov, A. Szanyi, P. Mizsey, Oxyfuel combustion makes carbon capture more efficient, ACS omega 9 (3) (2024) 3250–3261.

[6] X. Li, Z. Peng, Y. Pei, T. Ajmal, K.-J. Rana, A. Aitouche, R. Mobasheri, Oxy-fuel combustion for carbon capture and storage in internal combustion engines–a review, International Journal of Energy Research 46 (2) (2022) 505–522.

[7] J. Ferrari, Renewable fuels for long-term energy storage, Elsevier, 2021, pp. 109–138. doi:10.1016/b978-0-12-819873-5.00004-6.

[8] V. Dias, M. Pochet, F. Contino, H. Jeanmart, Energy and economic costs of chemical storage, Frontiers in mechanical engineering 6 (2020) 21.

[9] X. Rixhon, G. Limpens, H. Jeanmart, F. Contino, Taxonomy of the fuels in a whole-energy system, Frontiers in Energy Research 9 (2021) 660073.

[10] M. Ditaranto, J. Hals, Combustion instabilities in sudden expansion oxy–fuel flames, Combustion and flame 146 (3) (2006) 493–512.

[11] J. Serrano, J. Martín, J. Gómez-Soriano, R. Raggi, Theoretical and experimental evaluation of the spark-ignition premixed oxy-fuel combustion concept for future co2 captive powerplants, Energy conversion and Management 244 (2021) 114498.

[12] A. Van Blarigan, R. Seiser, J. Chen, R. Cattolica, R. Dibble, Working fluid composition effects on methane oxycombustion in an si-engine: Egr vs. co2, Proceedings of the Combustion Institute 34 (2) (2013) 2951–2958.

[13] P. C. T. de Boer, J.-F. Hulet, Performance of a hydrogen-oxygen-noble gas engine, International Journal of Hydrogen Energy 5 (4) (1980) 439–452.

[14] N. J. Killingsworth, V. H. Rapp, D. L. Flowers, S. M. Aceves, J.-Y. Chen, R. Dibble, Increased efficiency in si engine with air replaced by oxygen in argon mixture, Proceedings of the Combustion Institute 33 (2) (2011) 3141–3149.

[15] Z. Kang, S. Chen, Z. Wu, J. Deng, Z. Hu, L. Li, Simulation study of water injection strategy in improving cycle efficiency based on a novel compression ignition oxy-fuel combustion engine, SAE International Journal of Engines 11 (6) (2018) 935–946.

[16] A. Van Blarigan, D. Kozarac, R. Seiser, R. Cattolica, J.-Y. Chen, R. Dibble, Experimental study of methane fuel oxycombustion in a spark-ignited engine, Journal of Energy Resources Technology 136 (1) (2014) 012203.

[17] A. Van Blarigan, D. Kozarac, R. Seiser, J. Chen, R. Cattolica, R. Dibble, Spark-ignited engine nox emissions in a low-nitrogen oxycombustion environment, Applied energy 118 (2014) 22–31.

[18] S. Verhelst, R. Sierens, S. Verstraeten, A critical review of experimental research on hydrogen fueled si engines, SAE Transactions (2006) 264–274.

[19] P. Danieli, A. Lazzaretto, J. Al-Zaili, A. Sayma, M. Masi, G. Carraro, The potential of the natural gas grid to accommodate hydrogen as an energy vector in transition towards a fully renewable energy system, Applied Energy 313 (2022) 118843.

[20] B. Abraham, J. Asbury, E. Lynch, A. P. Teotia, Coal-oxygen process provides co/sub 2/for enhanced recovery, Oil Gas J.;(United States) 80 (11) (1982).

[21] R. Shaw, H. Oman, Non-air working fluids for closed-cycle diesel engines, in: Proc., Intersoc. Energy Convers. Eng. Conf.;(United States), Vol. 2, The Boeing Company, Seattle, Washington, 1983.

[22] M. Zheng, G. Reader, I. Potter, R. Gustafson, A thermodynamic model of an air-independent idi diesel engine system, Tech. rep., SAE Technical Paper (1992).

[23] J. Hawley, S. Ashcroft, M. Patrick, The design, construction and testing of a non air-breathing diesel engine research facility for autonomous underwater vehicle applications, Tech. rep., SAE Technical Paper (1992).

[24] J. Hawley, G. Reader, M. Zheng, I. Potter, O. Fraůvel, Investigations on carbon dioxide/oxygen breathing diesel engines—results from an international collaborative project, Underwater Technology 23 (3) (1998) 109–121.

[25] J. Hawley, G. T. Reader, Experimental performance results from a carbon dioxide/oxygen breathing diesel engine, SAE transactions (1994) 1757–1761.

[26] Z.-J. Wu, X. Yu, L.-Z. Fu, J. Deng, Z.-J. Hu, L.-G. Li, A high efficiency oxyfuel internal combustion engine cycle with water direct injection for waste heat recovery, Energy 70 (2014) 110–120.

[27] X. Yu, Z. J. Wu, Simulation on effect of egr on oxy-fuel ic engine, Applied Mechanics and Materials 130 (2012) 790–795.

[28] X. Yu, Z. Wu, L. Fu, J. Deng, Z. Hu, L. Li, Study of combustion characteristics of a quasi internal combustion rankine cycle engine, Tech. rep., SAE Technical Paper (2013).

[29] R. Abdel-Gayed, D. Bradley, F.-K. Lung, Combustion regimes and the straining of turbulent premixed flames, Combustion and Flame 76 (2) (1989) 213–218.

[30] D. Bradley, A. Lau, M. Lawes, F. Smith, Flame stretch rate as a determinant of turbulent burning velocity, Philosophical Transactions of the Royal Society of London. Series A: Physical and Engineering Sciences 338 (1650) (1992) 359–387.

[31] M. Pochet, H. Jeanmart, F. Contino, Uncertainty quantification from raw measurements to post-processed data: A general methodology and its application to a homogeneous-charge compression–ignition engine, International Journal of Engine Research 21 (9) (2020) 1709–1737.

[32] J. B. Heywood, Internal combustion engine fundamentals, McGraw-Hill Education, 2018.

[33] R. Abdel-Gayed, D. Bradley, M. Lawes, Turbulent burning velocities: a general correlation in terms of straining rates, Proceedings of the Royal Society of London. A. Mathematical and Physical Sciences 414 (1847) (1987) 389–413.

[34] R. Abdel-Gayed, K. Al-Khishali, D. Bradley, Turbulent burning velocities and flame straining in explosions, Proceedings of the Royal Society of London. A. Mathematical and Physical Sciences 391 (1801) (1984) 393–414.

[35] R. Abdel-Gayed, D. Bradley, M. Hamid, M. Lawes, Lewis number effects on turbulent burning velocity, in: Symposium (international) on combustion, Vol. 20, Elsevier, 1985, pp. 505–512.

[36] R. Abdel-Gayed, D. Bradley, Criteria for turbulent propagation limits of premixed flames, Combustion and Flame 62 (1) (1985) 61–68.

[37] R. Borghi, On the structure and morphology of turbulent premixed flames, in: Recent advances in the aerospace sciences: In honor of luigi crocco on his seventy-fifth birthday, Springer, 1985, pp. 117–138.

[38] N. Peters, Laminar flamelet concepts in turbulent combustion, in: Symposium (International) on combustion, Vol. 21, Elsevier, 1988, pp. 1231–1250.

[39] S. Kheirkhah, Ö. L. Gülder, A revisit to the validity of flamelet assumptions in turbulent premixed combustion and implications for future research, Combustion and Flame 239 (2022) 111635.

[40] S. Mohammadnejad, Q. An, P. Vena, S. Yun, S. Kheirkhah, Contributions of flame thickening and extinctions to a heat release rate marker of intensely turbulent premixed hydrogen-enriched methane-air flames, Combustion and Flame 231 (2021) 111481.

[41] X. Hu, Q. Yu, J. Liu, N. Sun, Investigation of laminar flame speeds of ch4/o2/co2 mixtures at ordinary pressure and kinetic simulation, Energy 70 (2014) 626–634.

[42] C.-W. Zhou, Y. Li, U. Burke, C. Banyon, K. P. Somers, S. Ding, S. Khan, J. W. Hargis, T. Sikes, O. Mathieu, et al., An experimental and chemical kinetic modeling study of 1, 3-butadiene combustion: Ignition delay time and laminar flame speed measurements, Combustion and Flame 197 (2018) 423–438.

[43] C. Ji, D. Wang, J. Yang, S. Wang, A comprehensive study of light hydrocarbon mechanisms performance in predicting methane/hydrogen/air laminar burning velocities, International Journal of Hydrogen Energy 42 (27) (2017) 17260–17274.

[44] T. Kar, Z. Zhou, M. Brear, Y. Yang, M. Khosravi, J. Lacey, A comparative study of directly injected, spark ignition engine combustion and energy transfer with natural gas, gasoline, and charge dilution, SAE International Journal of Fuels and Lubricants 15 (04-15-02-0009) (2022) 199–220.

[45] P. Abbasi Atibeh, M. J. Brear, P. A. Dennis, P. J. Orbaiz, H. C. Watson, Lean limit combustion analysis for a spark ignition natural gas internal combustion engine, Combustion science and technology 185 (8) (2013) 1151–1168.

[46] R. G. Abdel-Gayed, D. Bradley, A two-eddy theory of premixed turbulent flame propagation, Philosophical transactions of the royal society of London. Series A, Mathematical and physical sciences 301 (1457) (1981) 1–25.

[47] L. Gillespie, M. Lawes, C. Sheppard, R. Woolley, Aspects of laminar and turbulent burning velocity relevant to si engines, SAE transactions (2000) 13–33.

[48] D. Bradley, M. Shehata, M. Lawes, P. Ahmed, Flame extinctions: Critical stretch rates and sizes, Combustion and Flame 212 (2020) 459–468.